NANO · MICRO small
www.small-journal.com

The Effect of the 3D Nanoarchitecture and Ni-Promotion on the Hydrogen Evolution Reaction in MoS_2/Reduced GO Aerogel Hybrid Microspheres Produced by a Simple One-Pot Electrospraying Procedure

Jiajia Ran, Leonardo Girardi, Goran Dražić, Zhanhua Wang, Stefano Agnoli, Hesheng Xia, and Gaetano Granozzi*

The transition toward renewable energy sources requires low-cost, efficient, and durable electrocatalysts for green H_2 production. Herein, an easy and highly scalable method to prepare MoS_2 nanoparticles embedded in 3D partially reduced (pr) graphene oxide (GO) aerogel microspheres (MoS_2/prGOAMs) with controlled morphology and composition is described. Given their peculiar center-diverging mesoporous structure, which allows easy access to the active sites and optimal mass transport, and their efficient electron transfer facilitated by the intimate contact between the MoS_2 and the 3D connected highly conductive pr-GO sheets, these materials exhibit a remarkable electrocatalytic activity in the hydrogen evolution reaction (HER). Ni atoms, either as single Ni atoms or NiO aggregates are then introduced in the MoS_2/prGOAMs hybrids, to facilitate water dissociation, which is the slowest step in alkaline HER, producing a bifunctional catalyst. After optimization, Ni-promoted MoS_2/prGOAMs obtained at 500 °C reach a remarkable η_{10} (overpotential at 10 mA cm^{-2}) of 160 mV in 1 M KOH and 174 mV in 0.5 M H_2SO_4. Moreover, after chronopotentiometry tests (15 h) at a current density of 10 mA cm^{-2}, the η_{10} value improves to 147 mV in alkaline conditions, indicating an exceptional stability.

1. Introduction

Hydrogen has emerged as the most effective energy vector alternative to fossil fuels because of its high energy density and environmental sustainability, given that its only oxidation product is water.[1] To fulfil the requirements of the hydrogen economy,[2] a cheap route to green hydrogen production through water splitting (WS) must be developed, possibly using renewable energy sources (sun, wind...). One of the most promising WS processes involves electrolysis,[3] possibly photoassisted, and many efforts are currently taken to develop advanced electrocatalysts able to reduce the overpotential needed to dissociate water into molecular oxygen and hydrogen. The oxygen evolution reaction at the anode is still the bottleneck of the whole process, but there is also much room for the optimization of electrocatalysts for the hydrogen evolution reaction (HER) at the cathode side.[3–5] The most effective HER electrocatalysts, especially in acid conditions, are based on Pt-group metals (PGMs), which have a long story behind.[6] However, the current challenge is to develop highly active HER catalysts based on materials that are cheap and earth-abundant[7] and that can work in a variety of pH environments. Recently, remarkable advances have been made using transition-metal-dichalcogenides (TMDCs, e.g., MoS_2, $MoSe_2$, $MoTe_2$, WS_2...) as PGM-free HER electrocatalysts.[8–13] Their prototype is MoS_2, which has a relatively low hydrogen adsorption free energy at its edge sites or sulfur vacancies,[14] making it competitive with Pt. However, in MoS_2, both the activity of basal plane and the electron conductivity are rather low, which ultimately limit the overall electrocatalytic performances.[15] To overcome these hurdles, several strategies were proposed, e.g., the combination of MoS_2 with highly conductive materials and the optimization of structure and morphology to maximize the density of active sites.

Several studies sought to improve the electron transfer capabilities of MoS_2 by creating nanocomposites with various conductive materials, e.g., nanoporous carbons,[16] carbon

J. Ran, L. Girardi, S. Agnoli, G. Granozzi
Department of Chemical Sciences
University of Padova
Via F. Marzolo 1, Padova 35131, Italy
E-mail: stefano.agnoli@unipd.it
G. Dražić
Department of Materials Chemistry
National Institute of Chemistry
Hajdrihova 19, Ljubljana 1001, Slovenia
Z. Wang, H. Xia
State Key Laboratory of Polymer Materials Engineering
Polymer Research Institute
Sichuan University
Chengdu 610065, China
The ORCID identification number(s) for the author(s) of this article can be found under https://doi.org/10.1002/smll.202105694.

DOI: 10.1002/smll.202105694

nanotubes,[17] nanoporous metals,[18] or mesoporous graphene.[19] Even if significant advances were obtained, MoS_2 nanosheets are intrinsically prone to stack together during the synthesis, given their layered nature, severely limiting the number of the exposed catalytically active sites.[20] On the other hand, integrating MoS_2 nanosheets on 3D conductive porous scaffolds can enhance the electron transfer, while maintaining a high dispersion of the sheets because of the restricted movements allowed within the scaffold.[21] Following this idea, MoS_2 was grown on 3D graphene,[22,23] nickel foams[24–27] and silica[28] structures. The most common route to create such nanocomposites consists of mixing the 3D template with an exfoliated TMDC. However, in presence of an intrinsically irregular 3D template, some aggregation of the MoS_2 nanosheets can still persist, reducing the number of the exposed electrocatalytic sites, whereas the use of an ordered (i.e., with a narrow dispersion of pores) 3D template can partially fix this issue. In a p s paper,[29] we reported a successful route to disperse chemically exfoliated TMDC nanosheets within a graphene oxide (GO) aerogel having a special center-diverging microchannel 3D structure. These GO Aerogel Microspheres (GOAMs), with a radius of a few hundred micrometers, can be easily obtained by a bottom-up approach combining two subsequent steps, i) the electrospraying of GO suspensions and ii) the freeze-casting.[30] Interestingly, the microspheres maintain their shape even after a thermal reduction process (providing partially reduced GOAMs, prGOAMs). Adding exfoliated TMDCs during the GOAMs preparation step, TMDC/pr-GOAM hybrids were obtained, which kept their special morphology even during the electrochemical (EC) work and achieved better performance in the HER compared to electrodes built with the same materials, i.e., rGO and MoS_2, but without the 3D architecture with mesoscopic center diverging channels.

Herein, we make a step forward and propose a synthesis strategy to control not only the morphology of the nanocomposite, but also the chemistry of the active phase, realizing quite active bifunctional catalysts. To achieve this goal, we envisaged a fully bottom-up approach, which is based on a molecular precursor, e.g., ammonium tetrathiomolybdate (ATM, $(NH_4)_2MoS_4$)), to synthesize the MoS_2 phase decorating the 3D GOAM scaffold. The advantages of this approach to prepare the hybrid MoS_2/prGOAM materials are: i) fine and homogeneous dispersion of MoS_2 on the graphenic support, ii) higher scalability of the preparation procedure, and shorter preparation time since there is no need to prepare the TMDC by a lengthy and expensive exfoliation procedure, iii) possibility to introduce a large variety of promoting foreign metals into the MoS_2 moiety. The resulting materials with both tailored morphology and chemistry demonstrated to be outstanding catalyst for the HER, superior to previous top-down MoS_2 based catalysts[29] and similar catalysts found in the literature. In fact, the interaction at the molecular level of ATM with the oxygenated graphene surface, leads to the formation of intimately dispersed nanohybrids with a peculiar composition characterized by the presence of MoO_xS_y species, which according to previous works, promotes the electroactivity of the MoS_2 basal plane by narrowing the band gap[31] and guaranteeing an efficient electronic connection with the GO scaffold. Moreover, our bottom-up synthesis allows to introduce easily foreign metals into the growing MoS_2 phase, simply adding a soluble metal salt just before the electrospraying step.

A rich literature demonstrates that the modification of MoS_2 with foreign metals can be extremely beneficial for the electrocatalytic activity. As a case study we investigated the promotion effect of Ni (hereafter indicated as Ni-MoS_2/prGOAM), which has been widely investigated both theoretically [32] and experimentally [33] even though, different works connect the higher activity to different reasons such as formation of new phases,[33] substitutional doping with consequent modification of structural and electronic properties,[32] complex interaction with oxygen, and[34] change in the morphology.[35] This work therefore exemplifies the enormous potential of electrospray and freeze casting for the preparation of highly sophisticated electrocatalytic materials. This technique is extremely cheap and quick, very suitable to a rather fast and continuous production (e.g., hundreds of mg per hour of material produced with lab scale equipment). However, these extremely high productivity and cost effectiveness are not at the expenses of materials properties: as demonstrated here, a mesoporous hierarchical morphology perfectly suited for the interactions with electrolyte can be routinely realized and also the chemical composition can be tuned with high versatility, resulting in the synthesis of sophisticated nanocomposites designed at multiple scales.

2. Results and Discussion

The different materials tested in this work were prepared as described in the Experimental Section and summarized in **Scheme 1** (see the Experimental section for the sample labels). They were first structurally and chemically characterized by several physicochemical techniques and subsequently tested toward the HER both in acid and alkaline media.

2.1. Physicochemical Characterization

In the following we will most concentrate on the discussion of the physicochemical characterization of the Ni-MoS_2/prGOAM-40%-500 sample, which eventually resulted to be the best performing material for the HER.

As an example, **Figure 1**a,c shows the scanning electron microscopy (SEM) micrographs of Ni-MoS_2/prGOAM-40%-500 where the typical spherical morphology of the materials (≈300 µm diameter) is easily recognizable. Furthermore, the inner microstructure of Ni-MoS_2/prGOAM-40%-500 can be clearly observed in Figure 1d,e, and consists of a highly porous network made up by randomly interconnected graphene sheets. Such structure, resembling a dandelion blowball, shows radially oriented microchannels and is the result of the uniform cooling of the $NiCl_2$/GO/ATM/ice microsphere, where the ice crystals grow in the radial direction triggering the self-assembly of $NiCl_2$/GO/ATM blocks, which may organize through electrostatic/dispersive interactions and hydrogen bonds.[29,30] The radially oriented microchannel structure is retained after the removal of the templating ice crystals during the lyophilization step. The SEM images at larger magnification (reported in Figure 1f), show that the Ni promoted MoS_2 nanoparticles

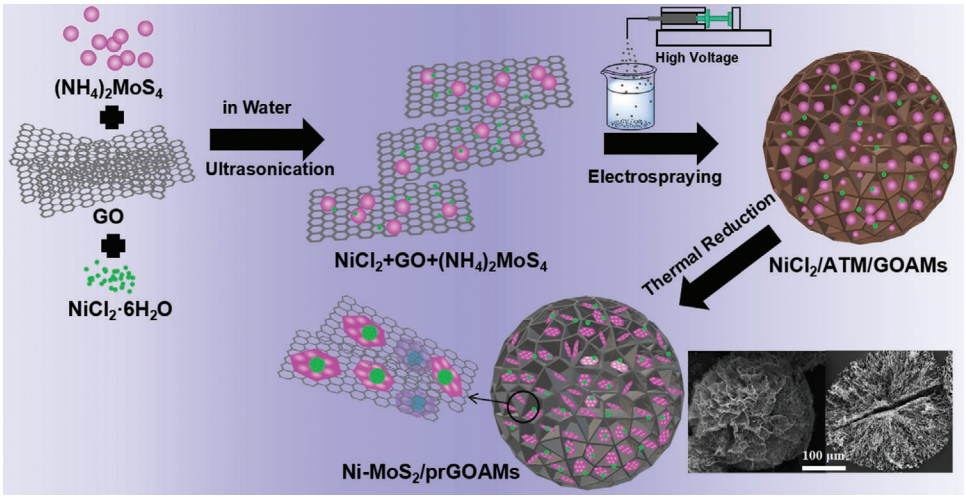

Scheme 1. Schematic illustration of the synthesis of the Ni-MoS_2/prGOAMs.

(vide infra), which typically exhibit a brighter contrast, are uniformly dispersed on the prGO surface. Such nanoparticles are often observed on GO wrinkles where sometimes they form larger aggregates, whereas on flatter GO sheets they show a variable size ranging between 20 and 80 nm. Figure 1g,h shows the SEM image and the corresponding energy dispersive X-ray spectroscopy (EDX) spectra. The total mass percentage of S and Mo is ≈39.6%, very close to the 40% value expected from the concentration in the precursor suspension, and the atomic ratio of Ni/Mo (5.7%) is very close to the nominal 5%, deriving from the precursor Ni:Mo ratio. Overall, the SEM/EDX investigation suggests that MoS_2 nanoparticles finely decorates the prGO sheets, which are efficiently interconnected creating a series of center diverging channels.

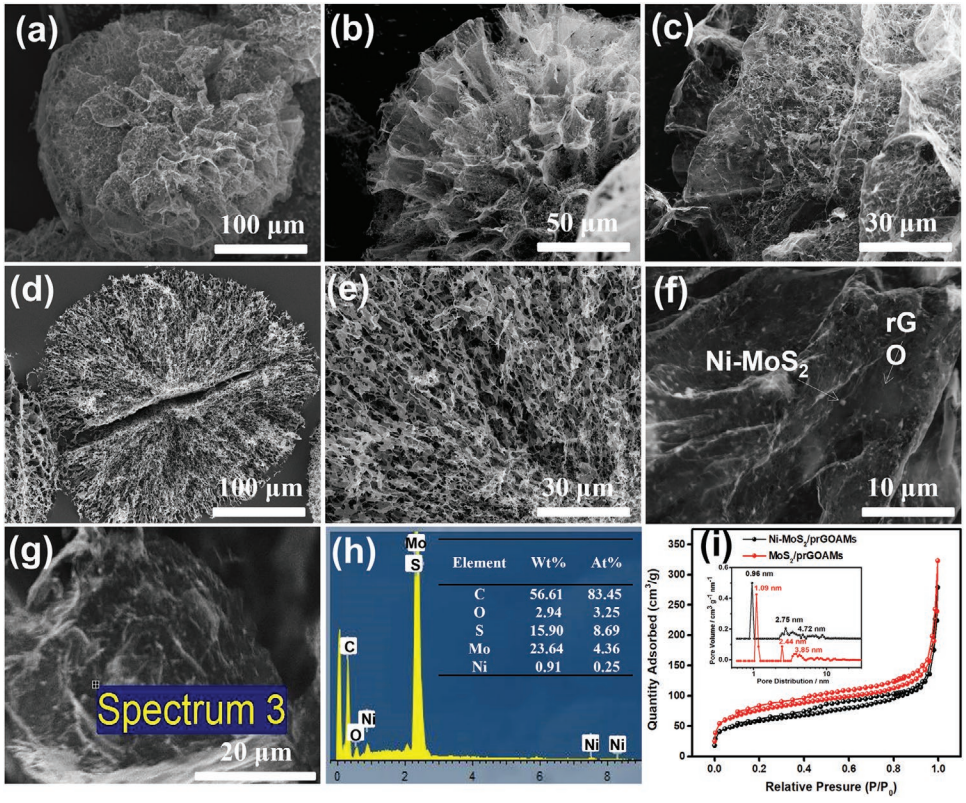

Figure 1. a–c) SEM images of typical Ni-MoS_2/prGOAM-40%-500 (a: lower magnification; b and c: higher magnification); d–f) Ni-MoS_2/prGOAM-40%-500 aerogel hemispheres made by cracking the microspheres; g,h) SEM image and EDX analysis of Ni-MoS_2/prGOAM-40%-500; i) N_2 adsorption–desorption isotherm and pore-size distribution (inset) of Ni-MoS_2/prGOAM-40%-500 and MoS_2/prGOAM-40%-500.

For comparison, Figure S1 in the Supporting Information, reports the morphology of the corresponding pristine MoS_2/prGOAM-40%-500 sample to verify that the introduction of the $NiCl_2$ in the precursor solution does not change the morphological features of the materials. In general, by varying the process parameters during the electrospraying process, MoS_2/prGOAMs with different average diameters can be obtained, e.g., 150 μm (V = 13 kV, rate = 10 mL h^{-1}), 200 μm (V = 12 kV, rate = 10 mL h^{-1}), 300 μm (V = 10 kV, rate = 8 mL h^{-1}) and 400 μm (V = 8 kV, rate = 8 mL h^{-1}) (Figure S2 in the Supporting Information), but they still retain the usual spherical shape and microchannel structure. Figure S3 in the Supporting Information shows the EDX spectrum of MoS_2/prGOAM-40%-500, which demonstrates again a good agreement between the nominal and experimental composition values.

The porosity of Ni promoted and pristine MoS_2/prGOAM-40%-500 was characterized using nitrogen adsorption experiments (Figure 1i). The N_2 adsorption–desorption isotherm of all samples showed a type IV isotherm (according to the IUPAC classification) with a small H3 hysteresis loop extending from P/P_0 = 0.45 to 0.95, demonstrating the presence of a mesoporous structure and slit-shaped pores,[36] as expected from the observed morphology. The N_2 adsorption–desorption measurements revealed that the as-prepared Ni decorated and pristine MoS_2/prGOAM-40%-500 hybrid with the diameter of 300 μm had Brunauer–Emmett–Teller (BET) specific surface area of 166 and 170 m^2 g^{-1}, respectively, which are slightly higher values than those obtained for 150 μm (144 m^2g^{-1}), 200 μm (151 m^2g^{-1}), and 400 μm (125 m^2g^{-1}) microspheres (Figure S4, Supporting Information). Moreover, MoS_2/prGOAMs (same diameter of ≈300 μm) with different weight percentage of MoS_2 have slightly different BET specific surface area (Figure S5, Supporting Information). The pore-size distribution of Ni containing and pristine MoS_2/prGOAM-40%-500 (300 μm) exhibit a dominant feature around 0.9–1.1 nm, and other weaker features at 2.4–5 nm (inset of Figure 1i), suggesting the presence of both micro- and mesopores. As a result of the BET analyses, we can deduce that the diameter of prGOAMs maximizing the surface area, is 300 μm, therefore in the following we will focus on this class of materials.

Figure 2a shows the X-ray diffraction (XRD) pattern of the Ni-MoS_2/prGOAM-40%-500 sample. The diffraction peaks at 33.0°, 39.6°, and 58.2° correspond to the (100), (103), and (110) planes of 2H-MoS_2, respectively. In the diffraction pattern, weak reflections associated with the formation of a $Ni_xMo_6S_8$ chevrel phase, i.e., a nonstoichiometric mixed metal sulfide, which can often exchange sulfur atoms for oxygen atoms, can be identified as well.[37] In fact, the possibility for both Ni and O to enter the lattice of MoS_2 is also confirmed theoretically: Ni atoms can substitute Mo atoms to occupy the transition metal lattice sites in Ni-doped MoS_2,[32] meanwhile Ni and O atoms can be co-present into MoS_2 nanosheets.[38]

Figure S6 in the Supporting Information shows the XRD pattern of the MoS_2/prGOAM-30%-500 and MoS_2/prGOAM-40%-500 samples, showing clear diffraction features associated with 2H-MoS_2. It is worth noticing that the intensity of (002) plane peaks of 2H-MoS_2 decreases with increasing the graphene amount in the composites, and MoS_2/prGOAM-40%-500 exhibits a larger interlayer spacing than MoS_2/prGOAM-30%-500 as suggested by the shift of (002) diffraction peak from 12.9° to 12.7°. This indicates that graphene inhibits the (002) plane growth of MoS_2 crystals in the hybrids.[39] Finally, the presence of the peak at ≈26.0° confirms that GO has been converted to prGO.

The characteristic Raman peaks of 2H-MoS_2 corresponding to the E^1_{2g} in-plane vibrational mode at 376 cm^{-1} and the A^1_g out-of-plane vibrational modes at 402 cm^{-1} are observed for MoS_2/prGOAM-40%-500 (Figure S7, Supporting Information),[40,41] in agreement with the XRD data. The ratio between the D and G peak intensity (I_D/I_G) gives important information about the disorder degree and defectivity of the carbon lattice:[42] the I_D/I_G of ATM/GOAMs was 0.96, smaller than that of MoS_2/prGOAMs (I_D/I_G = 1.3), which means that there are more defects after the high temperature treatment, which is not unusual in carbon materials and it is due to the formation of small new patches of C sp^2.[43]

Figure 2c shows the XPS C 1s region of Ni containing MoS_2/prGOAM-40%-500: different chemical species can be identified, i.e., C sp^2 at a binding energy (BE) of 284.2 eV, C sp^3 at 285.6 eV, C—O (epoxides and alcohols) at 286.9 eV, C=O (carbonyls) at 288.0 eV, HO—C=O (carboxyls) at 289.5 eV and the π–π* satellite at 290.9 eV. The observed relative intensity among the chemically shifted components suggests that the GO sheets have been substantially reduced during the thermal treatment (see for comparison Figure S8a in the Supporting Information for the materials before the annealing). The S 2p region (Figure 2d) presents two doublets: the former with maxima at 161.5 eV ($2p_{3/2}$) and 162.6 eV ($2p_{1/2}$) is ascribed to Mo—S bonds, while the latter with maxima at 163.8 eV ($2p_{3/2}$) and 164.9 eV ($2p_{1/2}$) to Mo—S—O.[44,45] Two small additional peaks at 168.1 eV ($2p_{3/2}$) and 169.2 eV ($2p_{1/2}$) are due to traces of SO_4^{2-}.[46,47] Figure 2e shows the XPS data of the Mo 3d region of Ni containing MoS_2/prGOAM-40%-500. Apart from the peak at a BE of 225.9 eV, which is associated with the S 2s core levels of MoS_2, the remaining eight peaks, are assigned to four 3d doublets of chemically distinct Mo species. The two peaks at 228.7 ($3d_{5/2}$) and 231.9 eV ($3d_{3/2}$), are ascribed to 2H-MoS_2,[44,45,48,49] whereas the Mo $3d_{5/2}$ component at 232.6 eV can be assigned to Mo^{6+} oxidation state and the other peaks (Mo $3d_{5/2}$ at 230.1 and 231.6 eV) are due to MoS_3 and to an oxysulfide phase MoO_xS_y, with an effective oxidation state of ≈ 5.5^+,[31] in agreement with the analysis of the S 2p spectrum. The oxysulfide phases is likely formed at the edges of MoS_2, either after environmental oxidation or, most likely, as intrinsic contaminant of the $Ni_xMo_6S_8$ chevrel phase, and especially at the interface with oxygenated species typical of GO and prGO, forming C—O—Mo bonds, which have shown to guarantee high structural stability and excellent electronic connection between the graphenic support and the TMDC.[50] Also the Ni $2p_{3/2}$ photoemission line (in Figure 2f) was separated into chemically shifted components taking into account the multiplet structure of Ni^{2+} ions:[51] the set of three peaks at lower BE, which account for 29% of the whole photoemission intensity is attributed to nickel ions in a mostly sulfur environment, i.e., NiS_xO_y, whereas the multiplet triplet centered at higher binding energy to NiO_x.[33,52] Above 860 eV, it is possible to observe a complex satellite structure, which is due to final state effects and it is typical of Ni^{2+} ions bonded to ligands capable of charge transfer screening such as oxygen and sulfur. It is worth nothing that the whole photoemission spectrum of Ni is shifted toward higher binding

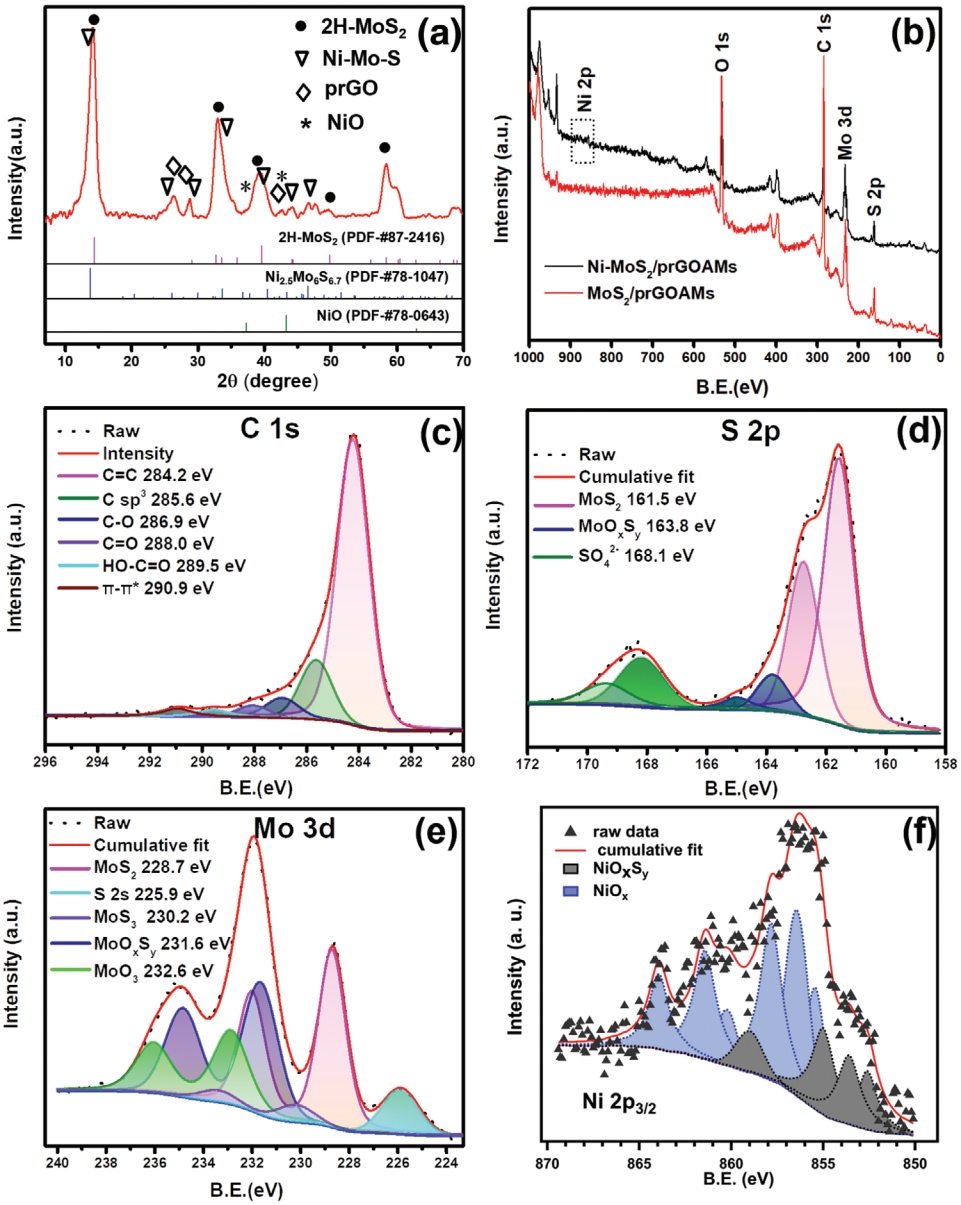

Figure 2. a) XRD pattern of Ni-MoS_2/prGOAM-40%-500; b) XPS broad survey spectrum of Ni- and pristine MoS_2/prGOAM-40%-500; XPS data of the C 1s (c), S 2p (d), Mo 3d (e), and Ni 2p (f) regions where the different fitted components are outlined.

energy compared to bulk NiO, indicating the existence of a charge transfer from interfacial Ni 3d levels to MoS_2 as rationalized by DFT calculations.[53]

Table 1 summarizes the atomic percentage of the different elements in Ni containing MoS_2/prGOAM-40%-500 derived from the photoemission data. The mass percentage of O and C atoms are 10.55% and 42.25%, respectively, and the total mass of S and Mo is 46.4%. In addition, the measured atomic ratio of Mo:S (1:2.5) is close to the MoS_2 stoichiometric value and the atomic ratio of Ni/Mo (5.3%) is very close to the nominal 5%.

We have also investigated by XPS the pristine MoS_2/prGOAM-40%-500 (Figure S9 and Table S2, Supporting Information). Regarding the Mo3d region, we can observe the same chemically shifted components of the Ni promoted sample: the Mo $3d_{5/2}$ peak at 228.8 eV can be assigned to Mo^{4+}, whereas, the other two Mo $3d_{5/2}$ peaks at 229.8 and 231.4 eV having much lower intensities, arise from the chemical environment of Mo atoms in MoS_3[54] and in a mixed MoO_xS_y phase. Notably in this case the peak associated with MoO_3 is completely absent, moreover the relative intensity of the chemically shifted component related to the oxysulfide phase (Table S3 in the Supporting Information) is much higher in the Ni promoted sample compared to the pristine material, suggesting that the presence of nickel strongly enhances the incorporation of oxygen into the MoS_2 lattice. Similar considerations can be also deduced inspecting the S 2p, (Figure S9b, Supporting Information) This behavior is not unexpected considering the high oxophilicity of nickel atoms. Finally, the analysis of the C

Table 1. The atom and mass percentages of different elements in Ni-MoS_2/prGOAM-40%-500 derived from XPS data.

Element	Atom percentage [%]	Mass percentage [%]
C	68.53	42.25
O	14.18	10.55
S	12.17	24.61
Mo	4.86	21.81
Ni	0.26	0.78

1s energy region confirms that GO was partially reduced and MoS_2 was successfully synthesized.

The multipeak analysis of the C 1s photoemission spectrum of the preheated ATM/GOAM sample is reported in Figure S8a in the Supporting Information. The O-related peaks in the C 1s region of MoS_2/prGOAM-40%-500 (e.g., C—O, C=O and O—C=O groups) have a much lower intensity, suggesting that after the heat treatment the GOAMs were reduced to a large extent to prGOAMs. In Figure S10 and Table S4 in the Supporting Information, we report the XPS data of MoS_2/prGOAM-30%-500: the total mass percentage of S and Mo are 30.7%, once again, confirming the good agreement between the expected and actual composition.

Figure 3 and Figure S11 in the Supporting Information show some typical high resolution (HR) transmission electron microscopy (TEM) data of the Ni-MoS_2/prGOAM-40%-500 sample.

The chemical maps indicate a homogeneous distribution of molybdenum, sulfur and nickel on the prGO surface with only the occasional formation of more contrasted areas, which indicate the presence of small aggregates. It can be seen an obvious correlation between the Mo and S signals as expected for MoS_2, but also a correlation with the signal of Ni, suggesting the formation of a $MoNi_xS_y$ solid solution. High-angle annular dark-field imaging (HAADF)-scanning transmission electron microscopic (STEM) images (Figure 3) clearly show the presence of crystalline nanosheets of MoS_2 of variable size, even as small as 2–3 nm, stacked on top of each other and characterized by disordered edges. On a closer look, single atomic defects (Figure 3d) can be identified, which on the basis of HAADF-STEM contrast simulations, can be associated with two types of surface defects, i.e., single Ni atoms either at regular threefold or interstitial sites. The presence of stable single atoms on the surface of MoS_2 on similar sites has been consistently reported in the case of several other transition metal atoms.[55,56]

For comparison, Figure S12 in the Supporting Information shows microscopic data of the Ni containing sample annealed at 900 °C. From the large area bright field image (Figure S12a, Supporting Information), the occasional formation of large nanoparticles (10–40 nm) is apparent. Based on the electron energy-loss spectroscopy (EELS) chemical maps, these features can be associated with both MoS_2 and nickel rich phases, either a Ni–Mo sulfide solid solution or Ni metal. Microdiffraction measurements (see inset in Figure S12a, Supporting Information) indeed show the presence of the diffraction features of metal Ni and MoS_2. Despite such sintering phenomenon, on a local scale HAADF-STEM images (Figure S12b, Supporting Information) show a situation very similar to the sample

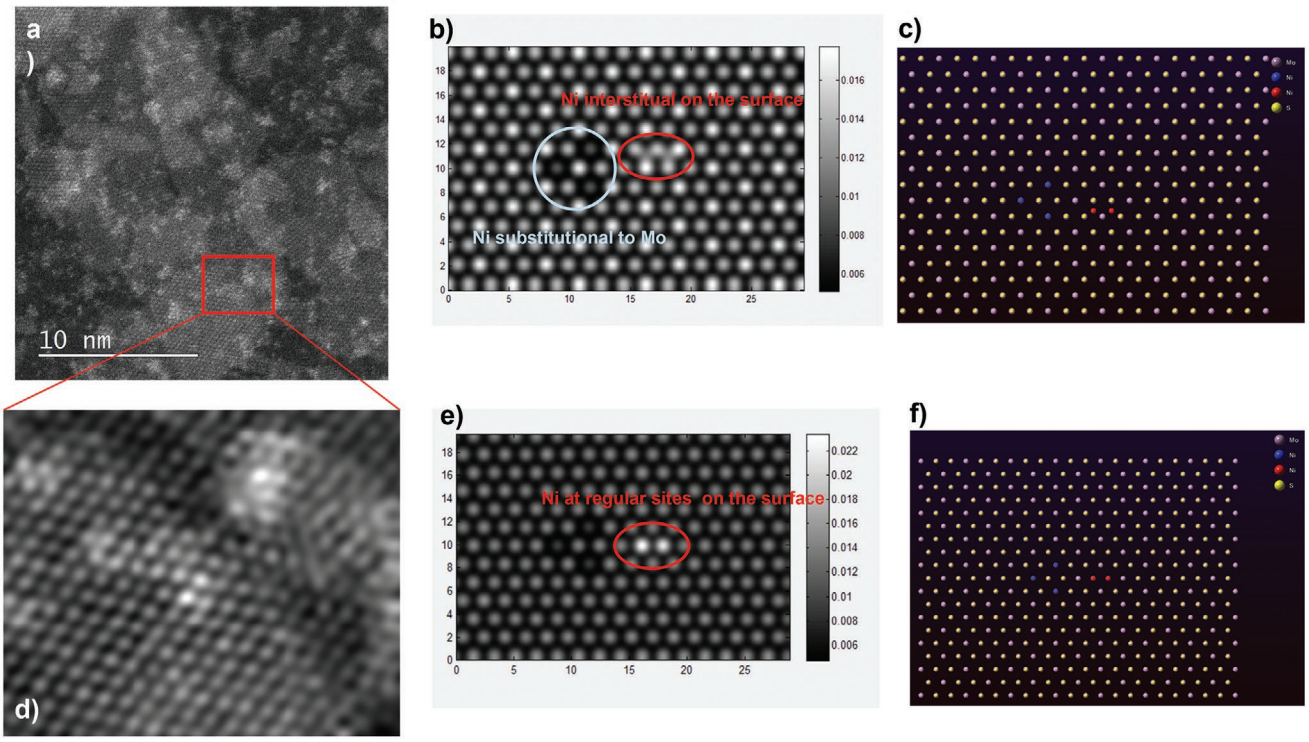

Figure 3. a) HAADF-STEM image of Ni-MoS_2/prGOAM-40%-500. b) Simulation of HAADF-STEM contrast for Ni single atoms on substitutional Mo sites or interstitial position on the surface according to the structural models shown in (c). d) Noise corrected enlarged area of the red rectangle in (a). e) Simulations of HAADF-STEM contrast for Ni substitutional atoms on the surface according to the structural model shown in (f).

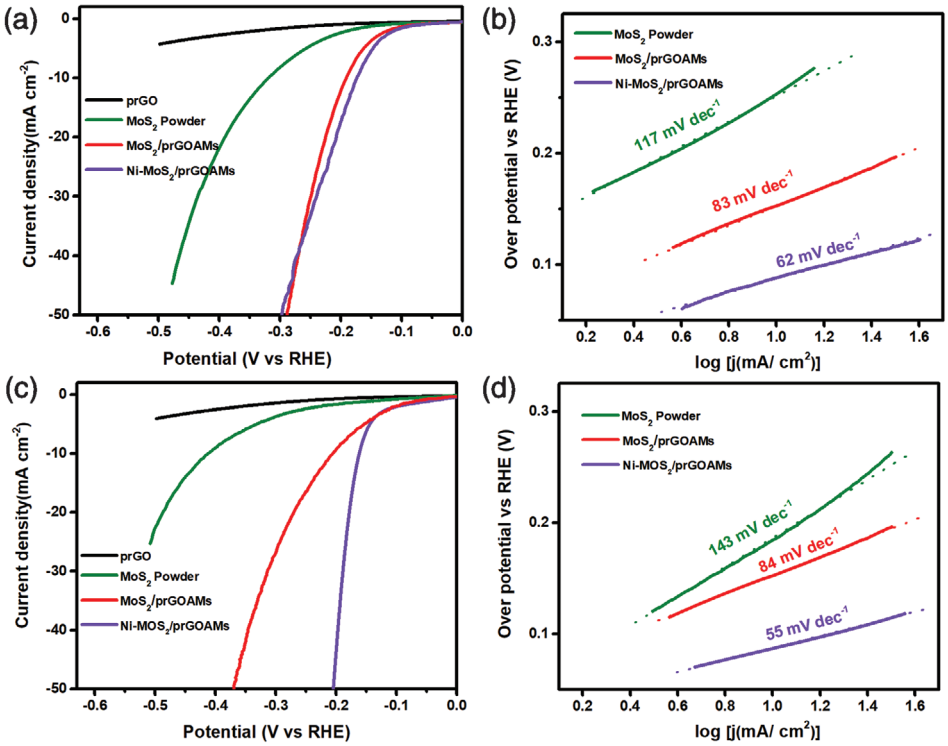

Figure 4. Polarization curves and Tafel plots in 0.5 M H_2SO_4 (a,b) and in 1 M KOH (c,d), respectively, for prGO, MoS_2 powder, MoS_2/prGOAM-40%-500, and Ni-MoS_2/prGOAM-40%-500.

annealed at lower temperature with small crystallites of MoS_2 in a very small size range (3–5 nm). Moreover, it is quite frequent to observe Janus structures made of nickel Nanoparticles supported on MoS_2 crystals suggesting the idea that the annealing at 900 °C produced a dealloying between MoS_2 and Ni. (Figure S13, Supporting Information) Finally, on this sample, given the loss of oxygen form the carbon support produced by the annealing at 900 °C, it is possible to observe a clear correlation between the EELS signal of Mo, S and O, confirming the formation of an oxysulfide as evidenced also by the XPS data.

In summary, the body of our experimental data suggests that Ni containing MoS_2/prGOAM-40%-500 is a rather complex nanocomposite: small MoS_2 nanosheets cover homogeneously the prGO nanosheets forming only occasionally large aggregates. Nickel is homogeneously dispersed either as single atoms located on the surface of the nanosheets, but also within, as deduced both by STEM–EDX chemical mapping and macroscopic XRD and XPS data. Finally, the correlation between Mo, S, and O chemical maps implies the formation of an oxysulfide substantiating the information provided by S 2p and Mo 3d spectra. After annealing at 900 °C, this nanocomposite undergoes partial sintering and becomes chemically unstable, and a nickel rich phase precipitates on the surface of MoS_2.

2.2. HER Electrocatalytic Characterization

To identify the active phases, and understand the role of the morphology and structure of the 3D template, we adopted a reductionist approach and investigated both in alkaline and acid conditions the HER activity of different composite systems, (**Figure 4**), i.e., prGO, prGO, and MoS_2 physically mixed powder, MoS_2/prGOAM-40%-500, and Ni-MoS_2/prGOAM-40%-500. The Ni-MoS_2/prGOAM-40%-500 sample presents the best HER activity with the lowest η_{10} (i.e., the overpotential necessary to reach a current density of 10 mA cm^{-2}) value of 174 mV versus reversible hydrogen electrode (RHE) in 0.5 M H_2SO_4 and 160 mV versus RHE in 1 M KOH, compared with the prGO+MoS_2 physically mixed powder (η_{10} of 325 mV vs RHE in 0.5 M H_2SO_4 and 416 mV vs RHE in 1 M KOH) and MoS_2/prGOAM-40%-500 (η_{10} of 189 mV vs RHE in 0.5 M H_2SO_4 and 206 mV vs RHE in 1 M KOH). In Figures S14 and Figure S15 in the Supporting Information, we report the morphologies of Ni- and pristine MoS_2/prGOAM-40%-500 after the HER activity test: both samples maintain their spherical shape and porous network features.

The same conclusions are reached when another figure of merit is taken into consideration, i.e., the Tafel slope, which is often utilized to evaluate the efficiency of the HER.

The linear portions of the Tafel plots (Figure 4b,d) were fit to the Tafel equation ($\eta = b \log j + a$), where j is the current density and b is the Tafel slope).[57–59] In acid conditions, the Ni-MoS_2/prGOAM-40%-500 exhibits a Tafel slope of 62 mV dec^{-1}, which is lower than that of MoS_2/prGOAM-40%-500 (83 mV dec^{-1}) and prGO+MoS_2 powder (117 mV dec^{-1}). In alkaline medium, the Ni-MoS_2/prGOAM-40%-500 exhibits a Tafel slope of 55 mV dec^{-1}, which is smaller than MoS_2/prGOAM-50%-500 (84 mV dec^{-1}) and prGO+MoS_2 physically mixed powder (143 mV dec^{-1}).

In the acidic media, the HER reaction proceeds through three principal reaction steps

Volmer adsorption step

$$H_3O^+ + e^- \rightarrow H_{ad} + H_2O \quad (1)$$

Heyrovsky desorption step

$$H_{ad} + H_3O^+ + e^- \rightarrow H_2 + H_2O \quad (2)$$

Tafel recombination step

$$2H_{ad} \rightarrow H_2 \quad (3)$$

In alkaline medium, the reaction proceeds as it follows:

Volmer adsorption step

$$H_2O + e^- \rightarrow H_{ad} + OH^- \quad (4)$$

Heyrovsky desorption step

$$H_{ad} + H_2O + e^- \rightarrow H_2 + OH^- \quad (5)$$

Tafel recombination step

$$2H_{ad} \rightarrow H_2 \quad (6)$$

where H_{ad} is the hydrogen adsorption site onto the surface of the catalyst. After the first Volmer step, there are two possibilities, i.e., Heyrovsky process, or Tafel recombination step. The expected value of the Tafel slope depends on the actual rate-determining step, and is 120 mV dec^{-1} for the Volmer step, and 40 and 30 mV dec^{-1}, for the Heyrovsky and Tafel ones respectively.[60–63] Therefore, the HER reaction for Ni-MoS_2/prGOAM-40%-500 and MoS_2/prGOAM-40%-500 likely follows a Volmer–Heyrovsky mechanism.

In general, the overpotential required to drive the overall reaction differs according to the reaction pathway, which is strongly dependent on the pH, and usually HER activity and exchange current densities are lower in alkaline rather than in acid solutions.[64–67] This is caused by the initial cleavage of the H—O—H bond in the Volmer step required in alkaline conditions (Equation (7)), which supplies H_{ad} to the following steps and is considered the rate-determining step of the overall reaction.[68] Also, in the MoS_2/prGOAMs samples we observed better catalytic figures of merit in acid medium compared to alkaline conditions. On the contrary, the electroactivity of Ni containing MoS_2/prGOAMs is significantly improved in alkaline conditions, likely because either Ni single atoms or NiO_xH_y clusters, which are formed by the reaction of Ni metal with the alkaline medium, supported on or within MoS_2, given their oxophilicity, can assist water adsorption and dissociation. The combination of MoS_2 and Ni based oxides or even single atoms (and more generally oxides of other transition metals) is not unusual in the literature. DFT calculations suggest that water is adsorbed either on the nickel single atom or nickel oxide aggregates and then it is electrochemically dissociated forming a hydroxide stabilized on nickel and a H adatom on MoS_2.[53,55,65,69] Microscopy, diffraction and spectroscopic data indicate that bifunctional NiO_xH_y/MoS_2 interfaces are extensively present in our materials.

The key role of nickel is also apparent from electrochemical impedance spectroscopic (EIS) measurements reported in **Figure 5** and Figure S16 in the Supporting Information. The impedance spectra were fitted with an electric circuit model (ECM) where a resistance (of the solution) is in series with two Randle circuits (Figure 5b). Each Randle circuit consists of a resistance in parallel with a capacitor, which, in our case, is exchanged with a constant phase element (CPE) that accounts for the nonideal behavior of the charged interface. The first Randle circuit was associated with the porous nature of the electrode,[66] and the other one with the charge transfer resistance (R_{CT}) related to the electrochemical reaction. The values of R_{CT} for each sample were obtained from a fitting procedure and are reported in Figure S17 in the Supporting Information as a function of the electrochemical potential.

Overall the Nyquist plots outline the presence of two semicircles: one at high frequencies, more evident in the Ni promoted samples, that is not significantly affected by the potential, which can be associated with the intrinsic electrical properties of the porous electrode, and another at low frequency that becomes smaller as the electrochemical potential

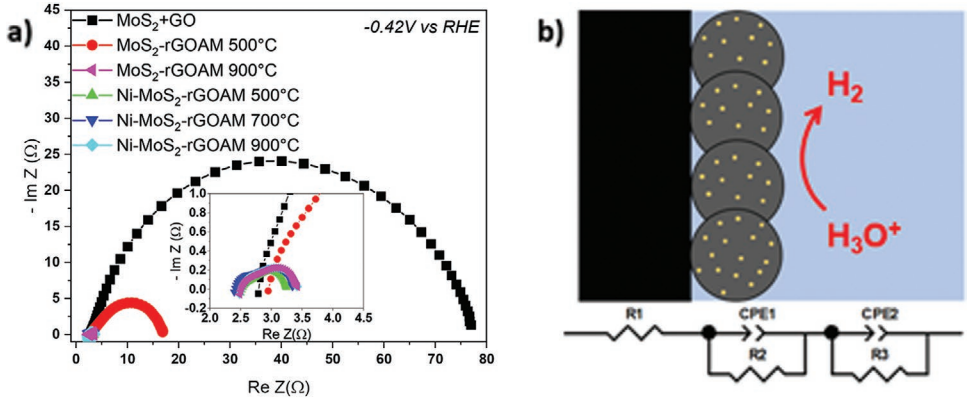

Figure 5. a) Nyquist plot acquired at –0.42 V for the different samples. b) Schematic representation of the equivalent electrical circuit model used to extract the charge transfer resistance.

is lowered, which therefore can be related to the charge transfer resistance for the HER.

From these data, we can deduce that the MoS_2 per se has poor charge transfer ability as demonstrated by the high R_{CT} observed for the physical mixture of MoS_2 and GO. The composite systems MoS_2/prGOAMs shows a strongly decreased R_{CT}, which is further lowered after annealing (from 500 to 900 °C). This indicates that the coupling of MoS_2 with a support with good electrical conduction effectively promotes the electrochemical transfer properties of the composite system. The situation is also strongly modified in presence of Ni: the comparison of the Ni promoted versus pure MoS_2/prGOAMs samples, both treated at 500 °C, shows huge differences in the R_{CT} and actually Ni promoted MoS_2/prGOAMs-500 °C is the best material in term of R_{CT}, even better than the analogous sample treated at 900 °C. This indicates that the promotion effect induced by nickel is more important than the improvement of electrical conductivity triggered by a higher annealing temperature, which improves the conduction properties of prGO. Moreover, when the whole set of Ni promoted samples is considered, the R_{CT} at potential lower than 0.124 V are almost the same no matter the annealing temperature is.

The previously discussed XPS and HRTEM data suggest that the presence of nickel induces as secondary effect the inclusion of oxygen atoms into MoS_2, eventually producing an oxysulfide. This incorporation of O has also an important effect on the HER, actually several papers report better electrocatalytic performances in case of samples incorporating oxygen.[31,70,71] In fact, DFT calculations indicate that substitutional oxygen produces a narrowing of the band gap of MoS_2, therefore enhancing the electron conductivity even in the case of highly defective samples with poor crystallinity.[31,70] Moreover, the presence of oxygen in MoS_2 can activate the basal plane increasing the electron density on the adjacent S atoms, which become chemically active facilitating the dissociation of water and assisting the first step of HER in alkaline conditions.[71]

From the R_{CT} values in the micropolarization region, it is also possible to extract the exchange current j_0, which is also used as metrics to evaluate the catalytic performance of electrodic materials. The results are reported in Table S5 in the Supporting Information and obviously mirror the trend observed for R_{CT}. The sample obtained by the physical mixing of MoS_2 and rGO has a j_0 of 4.3 μA cm^{-2}, whereas the best catalyst, Ni promoted MoS_2/prGOAMs-500 °C, a values that is 20 times higher.

These considerations are extendedly supported by the electrocatalysis experiments. Figure S18 in the Supporting Information compares the activity of Ni-MoS_2/prGOAM-40% samples, which were treated at different temperatures, namely 400, 500, 600, and 900 °C. The sample heated at 500 °C presents the best HER activity, with the lowest η_{10} value of 160 mV versus RHE in alkaline conditions. The same current density, in the case of 400, 600, and 900 °C electrodes can be only reached at significantly higher η_{10} values (243, 186, and 252 mV, respectively). The Tafel slopes (Figure S18b, Supporting Information) confirm the trend observed for η_{10}.

To determine if the optimal thermal treatment temperature changes without Ni, we also studied the dependence of the polarization curves of the pristine MoS_2/prGOAM-40% after different reduction temperatures (Figure S19, Supporting Information), obtaining the same trend observed in Ni-promoted samples. Probably, 500 °C is the best temperature because it is sufficient to form MoS_2 from the ATM precursor and significantly reduced the GO scaffold, but low enough to prevent sintering and aggregation of the active phase or an alteration of their stoichiometry and structure as indicated by the HRTEM measurements (Figures S12 and S13, Supporting Information). To support this hypothesis, we have evaluated the electrochemical surface area (ECSA) of the materials by measuring the capacitance of the double layer (C_{DL}), since these two quantities are usually assumed to be proportional. Cyclic voltammetry can be used to measure the C_{DL} at different scan rates in a potential region where there are no faradic processes. The most relevant results are reported in Figure S20 in the Supporting Information. Interestingly, MoS_2/prGOAMS sample shows a slightly higher ECSA than the analogous nickel promoted sample; however, the latter is much more active, stressing once more the fact that the nickel introduction promotes the formation of new and more active sites compare to the pure MoS_2. As expected by previous literature data on graphene-based composite, the annealing at high temperature determines a significant decrease of the surface area partly because of the sintering of MoS_2, but also due to the reduction of the GO, which leads both to a partial restacking of the nanosheets and a worse interaction with the electrolyte as a consequence of the increased hydrophobicity. Therefore, reduction of the ECSA explains the decrease of the catalytic performance observed in the samples treated above 500 °C, even though the annealing improves the electron transfer properties.

The key role played by Ni prompted us also to investigate the effect of its concentration in the HER performance, in particular we synthesized a series of samples with optimized parameters (MoS_2/prGOAM-40%-500) with different quantity of Ni: 2.5%, 5%, and 10% (Figure S21, Supporting Information). The enhancement of the catalytic activity in acid is radically different compared to alkaline conditions. Actually the experimental data suggest that the effect of nickel promotion is more evident and more sensibly dependent on the Ni amount in 0.1 M KOH compared to 0.5 M sulfuric acid.

Let us consider first what happens in acid conditions when, based on our electrocatalysis data, the enhancement of the catalytic activity is only modest and weakly dependent on the Ni loading. The TEM and XRD data suggest the existence Ni single atoms on the MoS_2 surface, or substitutional dopants inside the MoS_2 lattice (i.e., Chevrel phase). On the contrary on the basis of the pourbaix diagram, possible Ni metal islands are dissolved in acid conditions in the potential window of interest for the HER.

A large body of literature, as well as our own EIS data, indicate that the increase of the catalytic activity can be connected to enhanced electron transfer properties induced by the presence of Ni dopants as well as by the convenient modulation of the hydrogen adsorption energy, which is considered the best descriptor for the HER activity. In this regard DFT calculations suggest a more thermoneutral value of the hydrogen adsorption energy on Ni doped compared to pristine MoS_2 [55,69] or that the presence of Ni atoms can activate adjacent sulfur vacancies[72] or modulate locally the charge of the basal plane[32] favoring the HER.

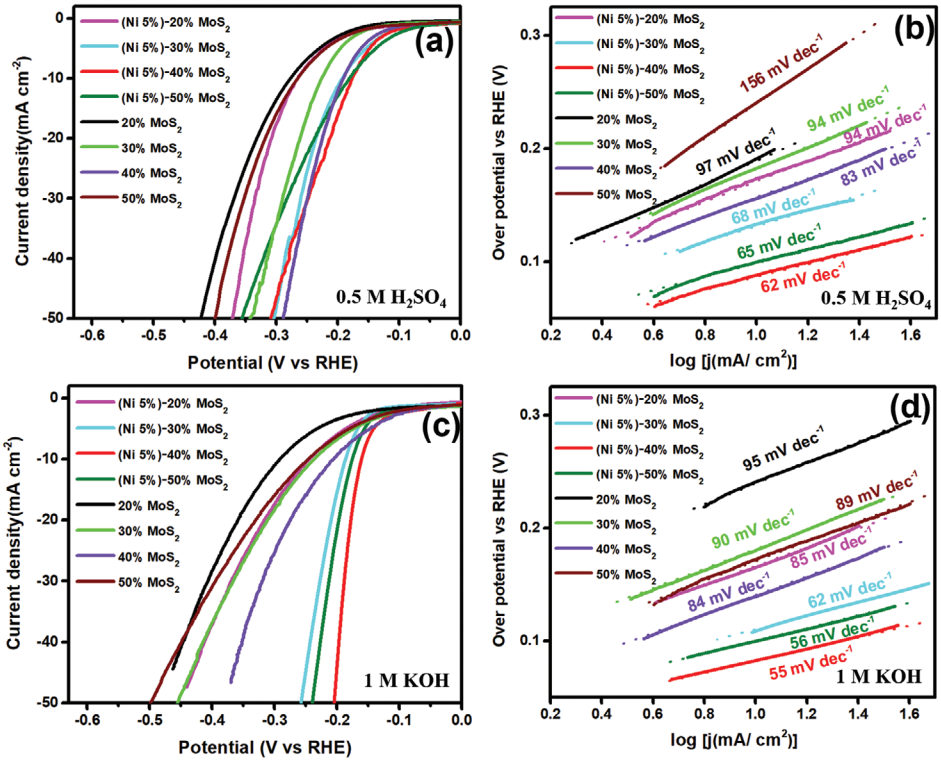

Figure 6. Polarization curves and Tafel plots in 0.5 M H_2SO_4 (a,b) and in 1 M KOH (c,d), respectively, for Ni-MoS_2/prGOAM-*x*%-500 and MoS_2/prGOAM-*x*%-500, (*x* = 20,30,40,50).

Clearly these effects are active also in alkaline conditions, at high pH, due to the low concentration of H^+, the rate determining step for the HER is the dissociation of water, which as discussed before can be indeed facilitated by oxophilic Ni species. Notably, in alkaline conditions the Ni metal nanoparticles are not dissolved but converted to $Ni(OH)_2$ which are also known to help water dissociation.

In all media, the best performing system contains 5% of Ni, whereas the less concentrated sample shows a similar activity and low overpotential, but worse performance at high currents, probably because of the reduced number of bifunctional sites. At 10% Ni, we observe a decreased of the performances, likely because the Ni increase does not produce additional sites, but just the formation of phase separated NiO_x phases as well as an excessive oxidation of the MoO_xS_y component.

The HER electrochemical activity of Ni promoted and pristine MoS_2/prGOAMs-*x*%-500 with different loading of MoS_2 was also evaluated. The η_{10} value of Ni-MoS_2/prGOAMs-*x*%-500 decreases from 262 mV to 174 mV (**Figure 6**a, in acid condition) and from 244 to 160 mV (Figure 6c, in alkaline condition) when the weight content of MoS_2 increases from 20% to 40%. This clearly indicates that the HER sites are related to MoS_2. However, when the MoS_2 loading is increased from 40% to 50%, η_{10} becomes slightly worse: changing from 174 to 179 mV (in acid condition) and from 160 to 178 mV (in alkaline condition), suggesting that the HER cannot indefinitely increase by adding more active phase. A similar trend can be deduced by the η_{10} values of the MoS_2/prGOAMs-*x*%-500 samples. These data suggests that the MoS_2 nanoparticles tend to aggregate and grew in size so that the TMDC/graphene interaction becomes less effective with respect to the electron transfer[67] and the addition of MoS_2 above 40% does not produce the exposure of additional active sites.

To facilitate the comparison of performance descriptors, Tafel slopes and η_{10} values are summarized in **Table 2**. It results that Ni promotes the activity in all the explored cases, decreasing the η_{10} and increasing the current density. However, the Ni presence is particularly advantageous when the HER is carried out in alkaline medium.

To assess the role of the special center diverging morphology of the microspheres, we prepared working electrodes using milled Ni(5%)-MoS_2/prGOAM-30%-500 and Ni(5%)-MoS_2/prGOAM-40%-500 powders. In both cases, the milled electrodes undergo a strong reduction of the catalytic performance (**Figure 7**a,b), especially in the case of the best catalyst, Ni-MoS_2/prGOAM-40%-500. This reduction is also evident in the pristine MoS_2/prGOAMs.

Finally, given its importance for practical applications, the long-term stability of the samples under HER working condition was investigated by chronopotentiometric measurements. Figure S22a,b in the Supporting Information shows the *V*–*t* curves of Ni-MoS_2/prGOAM-40%-500 sample obtained in alkaline and acid environment, respectively. As suggested by microscopy measurements (Figures S14 and S15, Supporting Information), the electrodes present a high stability in both pH conditions. However, in alkaline medium the catalytic activity increases slightly with time, while a low decrease is observed in acid conditions. Notably, at the end of the durability test,

Table 2. HER overpotentials at 10 mA cm^{-2} (η10) and Tafel slopes for the sample investigated ion the present study in 0.5 M H_2SO_4 and 1 M KOH.

Material	Overpotential η_{10} [mV]		Tafel slope [mV dec^{-1}]	
	0.5 M H_2SO_4	1 M KOH	0.5 M H_2SO_4	1 M KOH
prGO+MoS_2 powder	325	416	117	143
MoS_2/prGOAM-20%-500	273	289	97	95
MoS_2/prGOAM-30%-500	225	238	94	90
MoS_2/prGOAM-40%-500	189	206	83	84
MoS_2/prGOAM-50%-500	263	246	156	89
MoS_2/prGOAM-40%-400	317	297	148	120
MoS_2/prGOAM-40%-500	189	206	83	84
MoS_2/prGOAM-40%-600	289	285	117	99
MoS_2/prGOAM-40%-900	250	260	100	96
Ni(5%)-MoS_2/prGOAM-20%-500	262	244	94	85
Ni(5%)-MoS_2/prGOAM-30%-500	189	187	68	62
Ni(5%)-MoS_2/prGOAM-40%-500	174	160	62	55
Ni(5%)-MoS_2/prGOAM-50%-500	179	178	65	56
Ni(5%)-MoS_2/prGOAM-40%-400	–	243	–	98
Ni(5%)-MoS_2/prGOAM-40%-500	–	160	–	55
Ni(5%)-MoS_2/prGOAM-40%-600	–	186	–	63
Ni(5%)-MoS_2/prGOAM-40%-900	–	252	–	105
Ni(5%)-MoS_2/prGOAM-40%-900	–	252	–	105
Ni(2.5%)-MoS_2/prGOAM-40%-500	177	178	73	88
(Ni(10%)-MoS_2/prGOAM-40%-500	196	213	64	83

Ni-MoS_2/prGOAM-40%-500 exhibits an outstanding η_{10} of 147 mV, corresponding to a mass activity of 50 mA mg^{-1}, which is about twice higher than other similar materials recently reported in the literature (Table S6, Supporting Information), e.g., Co-MoS_2 (η_{10} 137 mV, 59 mV dec^{-1}, 28.6 mA mg^{-1})[68] and 1T-MoS_2/$Ni^{2+\delta}O^{\delta}(OH)^{2-\delta}$(1:1) ($\eta_{10}$ 73, 77 mV dec^{-1}, 25 mA mg^{-1}).[73] This comparison confirms the exceptional properties of the prGOAMs as supporting scaffold, which allows an extremely efficient utilization of the active phase. The reason for the improvement is related to a higher surface area (Figure S20, Supporting Information). Actually, the prGOAMs require some time to be fully permeated by the electrolyte because some of the pores are very small and the material surface is only partially hydrophilic. Moreover, the prGOAMs are produced by a soft ice templated method and the crosslinking between the GO sheets is due to dehydration reactions, which are partially reversible especially in alkaline conditions. Therefore, after some time in presence of electrolyte, the microspheres undergo swelling. Moreover, the H3 hysteresis type observed in BET spectra for these materials is typical of loosely aggregated plate like materials with slit shaped pores, confirming the "soft matter" nature of the prGOAMs.

Finally, Table S7 in the Supporting Information compares the figures of merits (η_{10} and Tafel slope) of the catalysts

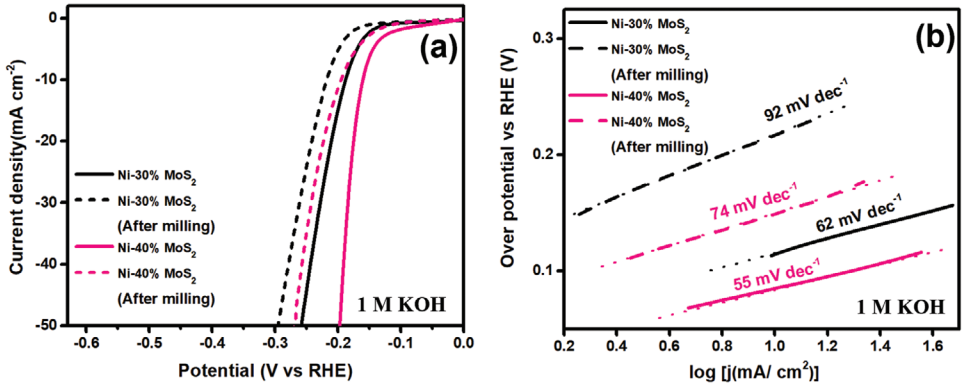

Figure 7. a) Polarization curves for Ni(5%)-MoS_2/prGOAM-30%-500 and Ni(5%)-MoS_2/prGOAM-40%-500 in 1 M KOH before and after milling; b) corresponding Tafel plots.

investigated in this work with other relevant literature data, where an active MoS_2 phase is supported on different 2D or 3D nickel or graphenic supports. The HER performance of the Ni(5%)-MoS_2/prGOAM-40%-500 catalyst compares very favorably to those observed for other non-noble-metal catalysts, e.g., 2D-MoS_2/$Ni(OH)_2$ (η_{10} 185 mV, 73 mV dec^{-1}),[65] MCM@MoS_2-Ni (η_{10} 263 mV, 82 mV dec^{-1}),[74] MoS_2–MoO_2 hybrids (η_{10} 240 mV, 76 mV dec^{-1}),[75] MoS_2 on 3D-Ni (η_{10} 237 mV, 110 mV dec^{-1}),[76] and Ni-3D-MoS_2 sample (η_{10} 220 mV, 65 mV dec^{-1}).[33]

Finally, considering the amount of MoS_2 deposited on the electrode and then converting this amount to the number of Mo sites exposed using the BET data, under the assumption based on TEM data that the prGO surface is almost completely covered by MoS_2, it is possible to calculate the turnover frequency (TOF),[32] which at –0.2 V results 0.9(1.2) s^{-1} for prGOAMs/MoS_2 and 4.6(1.8) s^{-1} for Ni promoted samples in alkaline (acid) conditions. Obviously these values represent the average value of all active sites (Ni promoted basal plane and edges).

These values are quite similar to previous data on closely related systems such as MoS_2/Ni_2O_3H, MoS_2/Co_3O_4, and MoS_2/Fe_2O_3 composite catalysts, whose TOFs are 2.0, 1.2, and 0.5 s^{-1} at the overpotential of 200 mV, respectively;[53] whereas for $Ni(OH)_2$/MoS_2, it was reported a TOF of 5 s^{-1} and for Ni doped MoS_2 a value of 60 s^{-1}.[32]

3. Conclusion

In conclusion, we have demonstrated the successful bottom-up fabrication of advanced nanocomposites made by MoS_2 nanosheets embedded in prGOAMs with a peculiar blowball morphology. This synthesis was possible through a facile and quick one-pot method that combines electrospraying and in situ freeze-drying technique.

The MoS_2/prGOAMs nanocomposites demonstrated a significant activity in the HER thanks to the special center diverging morphology of the carbon scaffold that guarantees a high dispersion of the active phase, and an efficient interaction with the electrolyte

However, the catalytic activity could be further boosted by the simple addition of a soluble nickel salt, $NiCl_2$, during the synthesis.

As a matter of fact, after a careful optimization procedure, the best material, Ni-MoS_2/prGOAM-40%-500, demonstrated an excellent performance especially in alkaline conditions, reaching an η_{10} of 140 mV even after 15 h of continuous electrolysis.

The presence of nickel during the synthesis produces important changes in the materials: on the one hand nickel is introduced into the MoS_2 both as dopant in the bulk forming the so called Chevrel solid solutions as demonstrated by XRD and as a single atom or small cluster on the surface as demonstrated by HRTEM measurements. Notably, XPS data suggest that the introduction of nickel strongly favor the formation of an oxysulfide phase, which has extremely beneficial effects on the electrochemical properties as demonstrated by the strong decrease of the charge transfer resistance in all Ni promoted samples. This can be explained considering that the oxygen atoms act as the bridging species between the oxysulfide and the oxygenates species of the prGO forming a structurally stable interface that allows an excellent electronic communication between the TMDC and the carbon support. Moreover, the oxysulfide phase per se has and improved electronic conduction compared to pure MoS_2 as well as an enhanced chemical activity on the sulfur atoms adjacent to the oxygen ones.

The nickel however has also a more direct role: in the form of single atom adsorbed on the surface, it is a good catalyst for the HER since it modifies the electronic properties of the basal plane, determining a more thermoneutral hydrogen adsorption energy compared to pure MoS_2.[55,69,72] On the other hand, nickel species in the form of oxysulfides or small oxidized clusters can establish a bifunctional effect.[53,55,65,69] where the oxofilic NiO_x species facilitate the electrochemical water dissociation providing a suitable adsorption site for hydroxyls intermediates,[77] whereas the surrounding MoS_x species can stabilize the resulting H atom and proceeds through the further steps of the HER.

Interestingly, given the high dispersion of Ni into MoO_xS_y the bifunctional effect is already achieved at a very low amount of nickel, 5% w/w only, which is much lower than similar NiO_xH_y/MoS_2 catalysts in the literature.[65,73,78] This point is quite important for practical application because nickel is not an environmental benign material, and its use should be minimized in practical applications.

4. Experimental Section

Synthesis of the MoS_2/prGOAMs and Ni-MoS_2/prGOAMs: Scheme 1 illustrates the synthetic route for the preparation of Ni-MoS_2/prGOAMs (Ni at 5 at% vs Mo). GO, $NiCl_2{\cdot}6H_2O$ and ammonium thiomolybdate (ATM) in different ratios were used to prepare a series of samples, which in the following are labeled as Ni-MoS_2/prGOAM-*X*-*Y* (where *X* indicates the weight percentage of MoS_2, and *Y* is the annealing temperature). GO, $NiCl_2{\cdot}6H_2O$ and ATM were added to 10 mL of deionized water, stirred and ultrasonicated at room temperature for 30 min to obtain a homogeneous suspension of 7.0 mg mL^{-1}. Table S1 in the Supporting Information summarizes the amount of the reagents used for the different samples. Starting from the precursor solution, a combination of electrospraying, ice templating, and thermal annealing was used for the synthesis of the Ni-MoS_2/prGOAMs composites. Regarding the electrospraying step, a beaker containing *n*-hexane was cooled down to –45 °C by an acetone/dry ice mixture and used as receiving liquid. Then, the $NiCl_2$/GO/ATM suspension was added to the injection pump of the electrospraying device, which was terminating with a small capillary (nozzle) connected to a high voltage power supply. After a careful optimization, the parameters for the electrospraying procedure were set within the following ranges: flow rate = 6–10 mL h^{-1}, high voltage = 9–12 kV, and distance between the receiving liquid and the nozzle = 8–12 cm. Microspheres with different diameters could be prepared by changing these parameters within these ranges. Under the action of the electric field, the electrically conductive suspension is stretched forming a "Taylor cone" and eventually splits into smaller charged droplets that enter the cooling bath, where they are rapidly frozen, producing $NiCl_2$/GO/ATM/ice microspheres. Finally, after rapid filtration, the solid microspheres collected in the cooled *n*-hexane bath were transferred to a freeze dryer working at –50 °C and less than 20 Pa, for 48 h, eventually obtaining the dried $NiCl_2$/ATM/GOAM microspheres ($NiCl_2$ and ATM inside the GOAM). Finally, the dried $NiCl_2$/ATM/GOAMs were heated to 400, 500, 600, or 900 °C under an Ar:H_2 = 9:1 (100 sccm in total) atmosphere for 1 h with a heating rate of 5 °C min^{-1}. The thermal

decomposition of ATM leads to molybdenum trisulfide (MoS_3), ammonia (NH_3), and hydrogen sulfide (H_2S), in the temperature range between 155 and 280 °C [79,80] according to the following reaction

$$(NH_4)_2MoS_4 \rightarrow MoS_3 + 2NH_3 + H_2S \quad (7)$$

MoS_3 then decomposes to MoS_2 in a broad temperature range from 300 to 820 °C under inert gas and hydrogen according to the following reaction[80]

$$MoS_3 + H_2 \rightarrow MoS_2 + H_2S \quad (8)$$

On the other hand, nickel chloride is reduced in a temperature range from 300 to 700 °C by hydrogen according to the reaction[81,82]

$$NiCl_2 + H_2 \rightarrow Ni + 2HCl \quad (9)$$

During the heat treatment, the GOAMs are also transformed into prGOAMs,[83] so the final Ni-MoS_2/prGOAMs are obtained. For the preparation of MoS_2/prGOAMs, the same procedure was followed simply without adding the $NiCl_2$ in the initial solution.

Structural and Morphological Characterizations: SEM measurements were carried out with a Zeiss Supra VP35 field-emission scanning electron microscopy (FE-SEM), equipped with in-lens, secondary electrons (SE), and backscattered electrons (BSE) detectors for the imaging (Zeiss, Jena, Germany). Micrographs were obtained with an acceleration voltage of 5 kV using in-lens high-resolution detection. EDX data were acquired with the same instrument. The surface area measurements were carried out with a Micromeritics ASAP 2020/2010 apparatus using the BET model for N_2 adsorption measurements. Prior to the adsorption run, the sample was outgassed at 573 K for 20 h.

XRD patterns were recorded in the diffraction angular range of 5–80° by a PANalytical X'Pert 3 diffractometer, working in the reflection geometry and equipped with a graphite monochromator on the diffracted beam (Cu Kα radiation, Pananlytical, Almelo, The Netherlands). Raman spectra were collected using a DXR Raman microscope system (Thermo Fisher Scientific, USA) with a 532 nm laser as the photoexcitation source, with 0.5 mW laser power at the sample and a 50× objective lens.

The surface chemical composition of the samples was investigated by XPS using a custom-made system working at a base pressure of 10^{-10} mbar and equipped with an EA 125 Omicron electron analyzer ending with a five channeltron detector. The XPS data were collected at room temperature using the Al Kα line ($h\nu$ = 1253.6 eV) of a non-monochromatized dual-anode DAR400 X-ray source. High resolution spectra were acquired using 0.1 eV energy steps, and 20 eV pass energy. The multipeak analysis of the C 1s, Ni 2p, Mo 3d, and S 2p photoemission lines was performed by means of Voigt functions and subtracting a Shirley background using the XPSPEAK software.

For microstructural investigations, probe Cs corrected STEM, Jeol ARM 200 CF, equipped with a high-brightness cold field emission gun (CFEG) operating at 80 kV was used. Elemental chemical analyses and elemental mappings were performed with energy dispersive X-ray spectroscopy (EDXS) using Jeol Centurio wide-area silicon drift detector system and EELS Gatan GIF Quantum ER Dual-EELS system. For HAADF, collection angles between 68 and 185 mrad were used. Samples in the powder form were directly transferred to Lacey-carbon coated Cu TEM grids.

HAADF image simulation was performed using QSTEM code.[84]

Electrochemical Characterization: The EC HER measurements were carried out in a custom designed three-electrode cell using an Autolab PGSTAT-204 potentiostat. Graphite was used as counter electrode, whereas an $Ag/AgCl_{(3M\ KCl)}$ electrode, calibrated with respect to the RHE, was the reference electrode. All potentials reported in the text and figures are referred to the (RHE) and corrected according to the equation: E(RHE) = E(Ag/AgCl) + 0.225 V + 0.059 pH. The EC experiments were carried out in Ar-saturated 0.5 M H_2SO_4 or 1 M KOH solution prepared from high-purity reagents (Sigma-Aldrich) and ultrapure Milli-Q water. The working electrodes were prepared by painting 100 µL of the catalyst ink (which was obtained by dispersing 1 mg of sample and 5 µL of Nafion in 200 µL of DMF, by ultrasonication for powder materials, whereas by gently shaking only for aerogel microspheres) on a 1 × 1 cm carbon cloth (Zoltek Tm PX30 Woven fabric, Hungary). The polarization curves were recorded at a 5 mV s^{-1} scan rate. The cycling stability measurements after CV experiments was performed for 1000 cycles with a scan rate of 50 mV s^{-1} in the potential range of –0.12 to –0.47 V (vs Ag/AgCl). The stability of the catalysts was tested by chronopotentiometry (CP) at 10 mA cm^{-2}. Curves were iR-corrected using the resistance determined by EIS.

EIS spectra were carried out using a modulation of 10 mV in a frequency range between 105 and 1 Hz using a Autolab PGSTAT204 (Metrohm, Utrecht, The Netherlands) instrument. The samples were polarized at different constant potential between –0.2 and –0.7 V versus Ag/AgCl (+0.230 V vs RHE) (0.08 to –0.42 V vs RHE).

Supporting Information

Supporting Information is available from the Wiley Online Library or from the author.

Acknowledgements

This research was funded by the Italian Ministry of Foreign Affairs and International Cooperation (MAECI, Grant PGR05249), Italian Ministry of University and Scientific Research (MIUR, PRIN 2015: SMARTNESS, 2015K7FZLH; PRIN2017: Multi-e, 20179337R7), and the National Science China Foundation (NSCF, Grant Number: 51861135201) through the Cooperation Project "GINGSENG" between Italy and China. J.R. acknowledges the financial support by the Chinese Scholar Council. Cariparo Foundation is acknowledged for funding (project Synergy, Progetti di Eccellenza 2018). G.D. acknowledges the financial support from Slovenian Research Agency (P2-0393, J2-3041).

Open access funding provided by Universita degli Studi di Padova within the CRUI-CARE Agreement.

Conflict of Interest

The authors declare no conflict of interest.

Data Availability Statement

The data that support the findings of this study are available from the corresponding author upon reasonable request.

Keywords

2D materials, hybrid materials, hydrogen evolution reaction, mesoporous materials, Ni-promotion

Received: September 17, 2021
Revised: January 23, 2022
Published online:

[1] A. S. Joshi, I. Dincer, B. V. Reddy, *Int. J. Hydrogen Energy* **2010**, *35*, 4901.
[2] N. P. Brandon, Z. Kurban, *Philos. Trans. R. Soc., A* **2017**, *375*, 20160400.
[3] Y. Jiao, Y. Zheng, M. Jaroniec, S. Z. Qiao, *Chem. Soc. Rev.* **2015**, *44*, 2060.
[4] I. Dincer, C. Zamfirescu, *Sustainable Hydrogen Prod.*, **2016**, 99. https://doi.org/10.1016/B978-0-12-801563-6.00003-0.

[5] M. G. Walter, E. L. Warren, J. R. McKone, S. W. Boettcher, Q. Mi, E. A. Santori, N. S. Lewis, *Chem. Rev.* **2010**, *110*, 6446.
[6] S. Trasatti, *Advances in Electrochemical Sciences and Engineering*, VOL *2*, (Eds: H. Gerischer, C. W. Tobias), Wiley, New York **1991**, pp. 1–85, Ch. 1.
[7] I. Roger, M. A. Shipman, M. D. Symes, *Nat. Rev. Chem.* **2017**, *1*, 0003.
[8] L. Lin, P. Sherrell, Y. Liu, W. Lei, S. Zhang, H. Zhang, G. G. Wallace, J. Chen, *Adv. Energy Mater.* **2020**, *10*, 1903870.
[9] Y. Kim, A. P. Tiwari, O. Prakash, H. Lee, *ChemPlusChem* **2017**, *82*, 785.
[10] M. R. Gao, J. X. Liang, Y. R. Zheng, Y. F. Xu, J. Jiang, Q. Gao, J. Li, S. H. Yu, *Nat. Commun.* **2015**, *6*, 5982.
[11] H. Wang, D. Kong, P. Johanes, J. J. Cha, G. Zheng, K. Yan, N. Liu, Y. Cui, *Nano Lett.* **2013**, *13*, 3426.
[12] D. Voiry, H. Yamaguchi, J. Li, R. Silva, D. C. B. Alves, T. Fujita, M. Chen, T. Asefa, V. B. Shenoy, G. Eda, M. Chhowalla, *Nat. Mater.* **2013**, *12*, 850.
[13] M. Chhowalla, H. S. Shin, G. Eda, L. J. Li, K. P. Loh, H. Zhang, *Nat. Chem.* **2013**, *5*, 263.
[14] B. Hinnemann, P. G. Moses, J. Bonde, K. P. Jørgensen, J. H. Nielsen, S. Horch, I. Chorkendorff, J. K. Nørskov, *J. Am. Chem. Soc.* **2005**, *127*, 5308.
[15] T. F. Jaramillo, K. P. Jørgensen, J. Bonde, J. H. Nielsen, S. Horch, I. Chorkendorff, *Science* **2007**, *317*, 100.
[16] Y. Liu, X. Zhou, T. Ding, C. Wang, Q. Yang, *Nanoscale* **2015**, *7*, 18004.
[17] D. J. Li, U. N. Maiti, J. Lim, D. S. Choi, W. J. Lee, Y. Oh, G. Y. Lee, S. O. Kim, *Nano Lett.* **2014**, *14*, 1228.
[18] Y. Tan, P. Liu, L. Chen, W. Cong, Y. Ito, J. Han, X. Guo, Z. Tang, T. Fujita, A. Hirata, M. W. Chen, *Adv. Mater.* **2014**, *26*, 8023.
[19] L. Liao, J. Zhu, X. Bian, L. Zhu, M. D. Scanlon, H. H. Girault, B. Liu, *Adv. Funct. Mater.* **2013**, *23*, 5326.
[20] Y. Zhao, J. Zhou, Z. Jia, D. Huo, Q. Liu, D. Zhong, Y. Hu, M. Yang, M. Bian, C. Hou, *Microchim. Acta* **2019**, *186*, 92.
[21] D. Wu, Y. Wang, F. Wang, H. Wang, Y. An, Z. Gao, F. Xu, K. Jiang, *Carbon* **2017**, *123*, 756.
[22] Q. Zhang, Z. Xu, B. Lu, *Energy Storage Mater.* **2016**, *4*, 84.
[23] F. Carraro, L. Calvillo, M. Cattelan, M. Favaro, M. Righetto, S. Nappini, I. Píš, V. Celorrio, D. J. Fermín, A. Martucci, S. Agnoli, G. Granozzi, *ACS Appl. Mater. Interfaces* **2015**, *7*, 25685.
[24] X. Geng, W. Wu, N. Li, W. Sun, J. Armstrong, A. Al-Hilo, M. Brozak, J. Cui, T. P. Chen, *Adv. Funct. Mater.* **2014**, *24*, 6123.
[25] W. Zhu, R. Zhang, F. Qu, A. M. Asiri, X. Sun, *ChemCatChem* **2017**, *9*, 1721.
[26] C. Tang, Z. Pu, Q. Liu, A. M. Asiri, Y. Luo, X. Sun, *Int. J. Hydrogen Energy* **2015**, *40*, 4727.
[27] A. P. Tiwari, Y. Yoon, T. G. Novak, K. S. An, S. Jeon, *ACS Appl. Nano Mater.* **2019**, *2*, 5061.
[28] J. Kibsgaard, Z. Chen, B. N. Reinecke, T. F. Jaramillo, *Nat. Mater.* **2012**, *11*, 963.
[29] M. Lunardon, J. Ran, D. Mosconi, C. Marega, Z. Wang, H. Xia, S. Agnoli, G. Granozzi, *Nanomaterials* **2020**, *10*, 2376.
[30] S. Liao, T. Zhai, H. Xia, *J. Mater. Chem. A* **2016**, *4*, 1068.
[31] X. Q. Bao, D. Y. Petrovykh, P. Alpuim, D. G. Stroppa, N. Guldris, H. Fonseca, M. Costa, J. Gaspar, C. Jin, L. Liu, *Nano Energy* **2015**, *16*, 130.
[32] R. Luo, M. Luo, Z. Wang, P. Liu, S. Song, X. Wang, M. Chen, *Nanoscale* **2019**, *11*, 7123.
[33] D. Mosconi, P. Till, L. Calvillo, T. Kosmala, D. Garoli, D. Debellis, A. Martucci, S. Agnoli, G. Granozzi, *Surfaces* **2019**, *2*, 531.
[34] D. Escalera-López, Y. Niu, J. Yin, K. Cooke, N. V. Rees, R. E. Palmer, *ACS Catal.* **2016**, *6*, 6008.
[35] A. P. S. Gaur, B. Zhang, Y. H. Lui, X. Tang, S. Hu, *Appl. Surf. Sci.* **2020**, *516*, 146094.
[36] Y. Tao, H. Kanoh, L. Abrams, K. Kaneko, *Chem. Rev.* **2006**, *106*, 896.
[37] C. L. Cang, Y. K. Tao, J. S. Swinnea, H. Steinfink, *Acta Crystallogr. C* **1987**, *43*, 1461.
[38] Y. Huang, Y. Sun, X. Zheng, T. Aoki, B. Pattengale, J. Huang, X. He, W. Bian, S. Younan, N. Williams, J. Hu, J. Ge, N. Pu, X. Yan, X. Pan, L. Zhang, Y. Wei, J. Gu, *Nat. Commun.* **2019**, *10*, 982.
[39] K. Chang, W. Chen, *ACS Nano* **2011**, *5*, 4720.
[40] J. E. Lee, J. Jung, T. Y. Ko, S. Kim, S. Il Kim, J. Nah, S. Ryu, K. T. Nam, M. H. Lee, *RSC Adv.* **2017**, *7*, 5480.
[41] D. Kong, H. Wang, J. J. Cha, M. Pasta, K. J. Koski, J. Yao, Y. Cui, *Nano Lett.* **2013**, *13*, 1341.
[42] J. Prasad, A. K. Singh, K. K. Haldar, V. Gupta, K. Singh, *J. Alloys Compd.* **2019**, *788*, 861.
[43] D. B. Schuepfer, F. Badaczewski, J. M. Guerra-Castro, D. M. Hofmann, C. Heiliger, B. Smarsly, P. J. Klar, *Carbon* **2020**, *161*, 359.
[44] H. Vrubel, D. Merki, X. Hu, *Energy Environ. Sci.* **2012**, *5*, 6136.
[45] H. W. Wang, P. Skeldon, G. E. Thompson, *Surf. Coat. Technol.* **1997**, *91*, 200.
[46] X. Zheng, J. Xu, K. Yan, H. Wang, Z. Wang, S. Yang, *Chem. Mater.* **2014**, *26*, 2344.
[47] A. Liu, L. Zhao, J. Zhang, L. Lin, H. Wu, *ACS Appl. Mater. Interfaces* **2016**, *8*, 25210.
[48] Y. H. Chang, C. Te Lin, T. Y. Chen, C. L. Hsu, Y. H. Lee, W. Zhang, K. H. Wei, L. J. Li, *Adv. Mater.* **2013**, *25*, 756.
[49] T. Weber, J. C. Muijsers, J. H. M. C. Van Wolput, C. P. J. Verhagen, J. W. Niemantsverdriet, *J. Phys. Chem.* **1996**, *100*, 14144.
[50] Y. Teng, H. Zhao, Z. Zhang, Z. Li, Q. Xia, Y. Zhang, L. Zhao, X. Du, Z. Du, P. Lv, K. Świerczek, *ACS Nano* **2016**, *10*, 8526.
[51] A. P. Grosvenor, M. C. Biesinger, R. St. C. Smart, N. Stewart McIntyre, *Surf. Sci.* **2006**, *600*, 1771.
[52] X. Y. Yu, Y. Feng, Y. Jeon, B. Guan, X. W. D. Lou, U. Paik, *Adv. Mater.* **2016**, *28*, 9006.
[53] J. Hu, C. Zhang, Y. Zhang, Q. Qi, B. Yang, M. Sun, F. Zi, M. K. H. Leung, B. Huang, *Small* **2020**, *16*, 2002212.
[54] T. Weber, J. C. Muijsers, J. W. Niemantsverdriet, *J. Phys. Chem.* **1995**, *99*, 9194.
[55] Q. Wang, Z. L. Zhao, S. Dong, D. He, M. J. Lawrence, S. Han, M. Gu, *Nano Energy* **2018**, *53*, 458.
[56] J. Li, S. Chen, F. Quan, G. Zhan, F. Jia, Z. Ai, L. Zhang, *Chem* **2020**, *6*, 885.
[57] D. Wang, X. Zhang, Y. Shen, Z. Wu, *RSC Adv.* **2016**, *6*, 16656.
[58] T. Kosmala, D. Mosconi, G. Giallongo, G. A. Rizzi, G. Granozzi, *ACS Sustainable Chem. Eng.* **2018**, *6*, 7818.
[59] A. Y. S. Eng, A. Ambrosi, Z. Sofer, P. Šimek, M. Pumera, *ACS Nano* **2014**, *8*, 12185.
[60] X. Dai, K. Du, Z. Li, M. Liu, Y. Ma, H. Sun, X. Zhang, Y. Yang, *ACS Appl. Mater. Interfaces* **2015**, *7*, 27242.
[61] S. Anantharaj, S. Noda, V. R. Jothi, S. C. Yi, M. Driess, P. W. Menezes, *Angew. Chem., Int. Ed.* **2021**, *60*, 18981.
[62] L. Wang, Y. Zhu, Z. Zeng, C. Lin, M. Giroux, L. Jiang, Y. Han, J. Greeley, C. Wang, J. Jin, *Nano Energy* **2017**, *31*, 456.
[63] B. Zhang, J. Liu, J. Wang, Y. Ruan, X. Ji, K. Xu, C. Chen, H. Wan, L. Miao, J. Jiang, *Nano Energy* **2017**, *37*, 74.
[64] J. Wei, M. Zhou, A. Long, Y. Xue, H. Liao, C. Wei, Z. J. Xu, *Nano-Micro Lett.* **2018**, *10*, 75.
[65] Z. Zhu, H. Yin, C. T. He, M. Al-Mamun, P. Liu, L. Jiang, Y. Zhao, Y. Wang, H. G. Yang, Z. Tang, D. Wang, X. M. Chen, H. Zhao, *Adv. Mater.* **2018**, *30*, 1801171.
[66] X. Yin, G. Sun, A. Song, L. Wang, Y. Wang, H. Dong, G. Shao, *Electrochim. Acta* **2017**, *249*, 52.
[67] X. Zhang, M. Zhang, Y. Tian, J. You, C. Yang, J. Su, Y. Li, Y. Gao, H. Gu, *RSC Adv.* **2018**, *8*, 10698.

[68] H. Duan, C. Wang, G. Li, H. Tan, W. Hu, L. Cai, W. Liu, N. Li, Q. Ji, Y. Wang, Y. Lu, W. Yan, F. Hu, W. Zhang, Z. Sun, Z. Qi, L. Song, S. Wei, *Angew. Chem.* **2021**, *133*, 7327.
[69] J. Ge, D. Zhang, Y. Qin, T. Dou, M. Jiang, F. Zhang, X. Lei, *Appl. Catal., B* **2021**, *298*, 120557.
[70] J. Xie, J. Zhang, S. Li, F. Grote, X. Zhang, H. Zhang, R. Wang, Y. Lei, B. Pan, Y. Xie, *J. Am. Chem. Soc.* **2013**, *135*, 17881
[71] J. Ge, D. Zhang, J. Jin, X. Han, Y. Wang, F. Zhang, X. Lei, *Mater. Today Energy* **2021**, *22*,1008546.
[72] J. J. L. Humphrey, R. Kronberg, R. Cai, K. Laasonen, R. E. Palmer, A. J. Wain, *Nanoscale* **2020**,*12*, 4459
[73] X. Zhang, Y. Liang, *Adv. Sci.* **2018**, *5*, 1700644.
[74] H. Zhang, L. Yu, T. Chen, W. Zhou, X. W. (David) Lou, *Adv. Funct. Mater.* **2018**, *28*, 1807086.
[75] L. Yang, W. Zhou, D. Hou, K. Zhou, G. Li, Z. Tang, L. Li, S. Chen, *Nanoscale* **2015**, *7*, 5203.
[76] K. Kim, A. P. Tiwari, G. Hyun, T. G. Novak, S. Jeon, *Int. J. Hydrogen Energy* **2019**, *44*, 28143.
[77] R. Subbaraman, D. Tripkovic, K. C. Chang, D. Strmcnik, A. P. Paulikas, P. Hirunsit, M. Chan, J. Greeley, V. Stamenkovic, N. M. Markovic, *Nat. Mater.* **2012**, *11*, 550.
[78] J. Liu, Y. Yang, B. Ni, H. Li, X. Wang, *Small* **2017**, *13*, 1602637.
[79] A. Müller, T. P. Prasad, R. Menge, Z.- J. Inorg, *Gen. Chem.* **1972**, *391*, 107.
[80] J. L. Brito, M. Ilija, P. Hernández, *Thermochim. Acta* **1995**, *256*, 325.
[81] W. F. G. R. H. Busey, *J. Am. Chem. Soc.* **1953**, *376*, 5.
[82] C. Hoang-Van, Y. Kachaya, S. J. Teichner, Y. Arnaud, J. A. Dalmon, *Appl. Catal.* **1989**, *46*, 281.
[83] L. S. Zhang, W. D. Wang, X. Q. Liang, W. S. Chu, W. G. Song, W. Wang, Z. Y. Wu, *Nanoscale* **2011**, *3*, 2458.
[84] C. T. Koch, *Ph.D. Thesis*, Arizona State University **2002**.